# C-V and I-V characteristics of quantum well varactors[a)]

J. P. Sun, R. K. Mains, W. L. Chen, J. R. East, and G. I. Haddad
*Center for High-Frequency Microelectronics, Solid State Electronics Laboratory, Department of Electrical Engineering and Computer Science, The University of Michigan, Ann Arbor, Michigan 48109*

(Received 5 March 1992; accepted for publication 21 May 1992)

A theoretical model for quantum well varactors is presented. The model is used to calculate the device *C-V* and *I-V* characteristics and very good agreement has been found between the calculated and measured results. Based on the model, a triple barrier double well varactor has been designed and fabricated. A very high capacitance ratio within a very small bias range is achieved, as designed. Details of the design calculations and experimental results are presented.

## I. INTRODUCTION

Quantum well varactors[1,2] are very attractive candidates for frequency multiplier applications with potentially superior performance compared to Schottky barrier varactors at millimeter and submillimeter wavelengths. The potential advantage of quantum well varactors lies in their symmetrical, highly nonlinear capacitance characteristics over a small bias range. The symmetrical device *C-V* characteristic eliminates the second harmonic component, resulting in more efficient harmonic conversion for frequency tripler applications.

Several novel varactor structures have been proposed and investigated over the last few years, including quantum barrier varactors (QBV) or single barrier varactors (SBV),[2] double barrier quantum well varactors (QWV),[3] barrier-intrinsic-N (BIN) structures, and barrier-N-$N^+$ (BNN) structures.[4] However, recent *C-V* measurements of quantum well varactors have shown that there are discrepancies between a simple model based on the depletion approximation and the experimental data,[2,3] and the devices so far fabricated show less nonlinearity than theoretically expected, with the capacitance ratio ($C_{max}/C_{min}$) typically being 2–3 within a bias voltage of 1–2 V. Some of these results are shown in Fig. 1.[2] Moreover, the simple model cannot predict the quantum-mechanical current density of the device which should be kept sufficiently low in order to minimize the circuit loss. In addition, it is difficult to optimize the device *C-V* characteristics in terms of the doping profile using the simple model.

In this article, we present a theoretical model for quantum well varactors based on a self-consistent calculation of the charge and potential distributions in the device. The electron concentrations in the contact regions are calculated using a Thomas–Fermi equilibrium approximation, while the concentration in the quantum barrier/well region is determined using a quantum calculation. The model can be used for the design of multiple quantum well varactors in terms of their *C-V* and *I-V* characteristics and for optimization in terms of device structure and doping profile.

A triple-barrier, double-well (TBDW) varactor has been designed and fabricated based on the model. In Sec. II, the formulation of the device model is outlined. The device design and fabrication are described in Sec. III. Section IV presents and discusses a comparison between the calculated and measured results, and the article is summarized in Sec. V.

## II. METHOD OF CALCULATION

### A. Self-consistent charge and potential distributions

For an accurate evaluation of the quantum mechanical current density and the dependence of the capacitance on the applied voltage of a quantum device structure such as the quantum well varactor in this work, a self-consistent solution to Poisson's equation and the Schrödinger equation is desired. However, a full self-consistent model based on the above equations has a conceptual difficulty in that the scattering mechanisms must be invoked to account for the band bending or the formation of an accumulation layer near the barrier.[5,6] However, if the current density is calculated by sending eigenstate electrons from the contacts, the pure state Schrödinger equation is not adequate to formulate the scattering processes. Therefore, quantum kinetic formalisms such as the Wigner function approach may have to be employed, which usually demand extensive computer resources and are not considered to be very suitable for routine analysis and design purposes. The device model of the quantum well varactor presented here is based on a self-consistent calculation of the potential and charge distributions in the device, similar to a model for the resonant tunneling diode,[7] in which the approximations and detailed discretized formulations have been described. To find the potential and charge distributions, the contact regions are treated using the Thomas–Fermi equilibrium model, i.e., carrier concentrations are obtained assuming constant Fermi levels within each contact, determined by the equilibrium Fermi–Dirac statistics. Within the barrier/well region, the electronic charge is obtained from an eigenvalue solution of the time-independent Schrödinger equation. When biased, the Fermi levels in the contact regions are separated by the applied bias voltage and connected by a linearly varying Fermi level in the barrier/well region. The concentration obtained inside the barrier/well region is then self-consistently coupled to the Thomas–Fermi model through matching conditions.

[a)]A part of the results has been presented at 1991 International Semiconductor Device Research Symposium, Charlottesville, VA, December 4–6, 1991. Proceedings of the 1991 ISDRS, University of Virginia, Charlottesville, VA, December 4, 1991, pp. 61–64.

 0021-8979/92/182340-07$04.00  

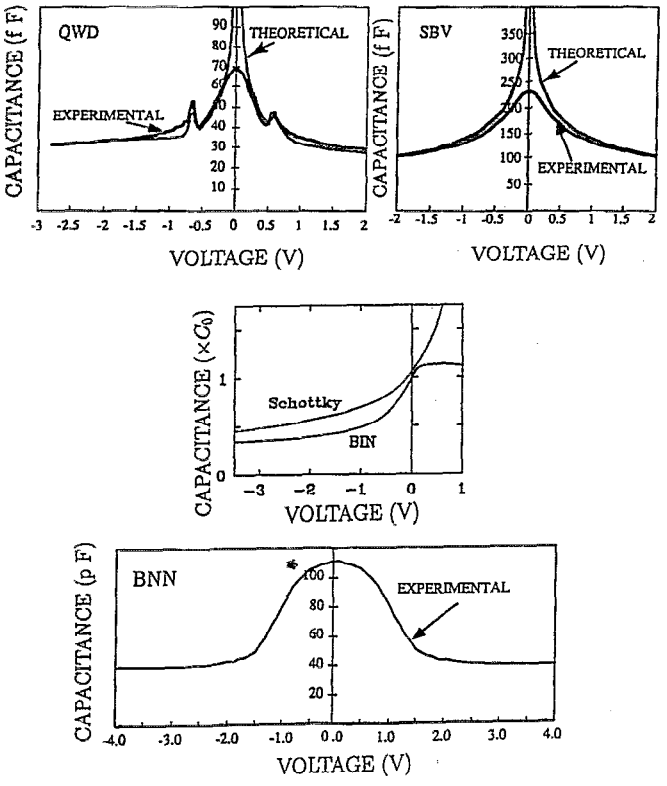


FIG. 1. $C$-$V$ characteristics for varactors of various structures from Ref. 2.

The device calculations can be divided into three parts, i.e., a Thomas–Fermi calculation and two quantum calculations, described as follows: For a varactor diode structure involving quantum barrier/well regions between two contact regions (cf. Fig. 3), the electron electrostatic potential and charge distributions of the device are related by Poisson's equation

$$\frac{\partial^2 V(x)}{\partial x^2}=-\frac{q}{\epsilon}[N_d(x)-n_e(x)], \tag{1}$$

and the electron concentration outside the barrier/well region can be expressed, within the Thomas–Fermi approximation, in terms of local Fermi levels,

$$n_e(x)=\int_0^\infty N(E)f(E)dE=N_c\frac{2}{\sqrt{\pi}}\int_0^\infty \frac{\chi^{1/2}d\chi}{1+e^{\chi-\eta}}, \tag{2}$$

where $N(E)$ is the density of states in the contact regions, and

$$f(E)=1\Big/\left[1+\exp\left(\frac{E-E_F}{k_BT}\right)\right]$$

is the Fermi–Dirac distribution function,

$$N_c=2[m_e^* k_BT/(2\pi\hbar^2)]^{3/2}$$

is the effective density of states in the conduction band, and

$$\chi=\frac{E-E_c(x)}{k_BT},\quad \eta=\frac{E_F-E_c(x)}{k_BT}.$$

Note that the Fermi levels are assumed to be constant, respectively, in the left and right contact regions and that the conduction band edge varies with distance in the contact regions according to:

$$E_c(x)=E_c(-\infty)-qV(x).$$

The Fermi integral in Eq. (2) can be expanded by a rapidly converging power series in terms of the ratio $r=n_e(x)/N_c$, based on an extension of the Joyce–Dixon approximation:[8,9]

$$\eta-\log r=\sum_{k=1}^{N}A_k r^k, \tag{3}$$

with the coefficients $A_k$ determined using a least-squares fit technique. Up to $N=12$ terms of the series are retained to yield the correct Fermi energy value accurate to within $10^{-4}$ eV at 80 K for the doping level in the contact regions. We now have

$$\eta=\frac{E_F-E_c(x)}{k_BT}\cong\log\left(\frac{n_e(x)}{N_c}\right)+\sum_{k=1}^{N}A_k\left(\frac{n_e(x)}{N_c}\right)^k. \tag{4}$$

Equation (2) is then written as

$$\log\left(\frac{n_e(x)}{N_c}\right)+\sum_{k=1}^{N}A_k\left(\frac{n_e(x)}{N_c}\right)^k =\frac{E_F-E_c(-\infty)}{k_BT}+\frac{qV(x)}{k_BT}, \tag{5}$$

where $V(x)$ will have to be consistent with the solution of Eq. (1). This leads to a pair of coupled nonlinear equations with two unknowns, i.e., the electronic charge and potential at every spatial point in the contact regions. The calculation to solve Eqs. (1) and (2) simultaneously is referred to as the Thomas–Fermi calculation, which is carried out using the Newton–Raphson iterative method with a sparse matrix technique. Note that the Thomas–Fermi calculation is *per se* a semiclassical treatment and the above procedure is used to determine $n_e(x)$ only outside the barrier/well region. For charge inside the quantum wells as well as the quantum mechanical current through the device, quantum calculations must be performed. Therefore, two quantum calculations are invoked; the first is an eigenvalue calculation for the charge in the quantum barrier/well region, and the second is a traveling wave calculation for the current density through the device. The eigenvalue calculation is performed using an eigenvalue solver to solve the Schrödinger equation with the assumption that the barrier/well region constitutes a closed system. We have performed transmission calculations for multiple quantum well structures with open boundary conditions; for the energies not very close to the top of the barriers, the eigenenergies obtained for the closed system match closely with the transmission peaks[10] and therefore represent a good approximation for the energy levels in the quantum wells. The traveling wave calculation will be discussed in Sec. II B.

For both of the quantum calculations, the time-independent Schrödinger (effective mass) equation is used:

$$-\frac{\hbar^2}{2}\frac{\partial}{\partial x}\left(\frac{1}{m^*(x)}\frac{\partial\psi(x)}{\partial x}\right)+E_c(x)\psi(x)=E\psi(x), \quad (6)$$

where $E_c(x)$ is the conduction band edge including the heterojunction potential offset and $m^*(x)$ is the spatially variable effective mass, both of which can be readily specified in a discretized scheme. The charge in the quantum wells is given by

$$n_{qw}(x)=\frac{m^*k_BT}{\pi\hbar^2}\sum_i \ln\left[1+\exp\left(-\frac{E_i-E_F(x)}{k_BT}\right)\right] \times|\psi_i(E_i,x)|^2, \quad (7)$$

where $i$ is the subband index in the quantum wells, and the Fermi level $E_F$ is taken to be linearly varying in the barrier/well region from the left contact to the right contact. The difference of the Fermi levels at the contacts is determined by the applied bias voltage.

The Thomas–Fermi calculation carried out previously and the quantum charge calculation are now coupled using matching conditions. These conditions express the fact that at the left and right boundaries of the barrier/well region, the discontinuity of electric field across the region is related to the integral of the charge inside, and that the potential discontinuity is related to this charge and the boundary electric fields. In addition, the potential in the quantum well(s) region between the contacts is modified according to the calculated space charge there. When convergence is achieved to a prescribed tolerance, the traveling wave calculation is performed to calculate the current density.

### B. Current density

In order to convert the three-dimensional electron distribution for a one-dimensional calculation, the electron wave function must be multiplied by a weighting function that effectively integrates over transverse wave vectors. The weighting function is given by

$$W(k_l)=\frac{1}{4\pi^3}\int_{-\infty}^{\infty}\int_{-\infty}^{\infty}f(E_l+E_t)d^2k_t =\frac{m^*k_BT}{2\pi^2\hbar^2}\ln\left[1+\exp\left(\frac{-(E_l-E_F)}{k_BT}\right)\right], \quad (8)$$

where $f(E_l+E_t)$ is the Fermi–Dirac distribution function, $E_l=\hbar^2k_l^2/2m^*$ is the longitudinal energy of the electron with wave-vector $k_l$, $E_t=\hbar^2k_t^2/2m^*$ is the transverse energy of the electron with $k_t$, and $k_t^2=k_y^2+k_z^2$ for $x$ being the growth direction. The current density through the device is calculated from the time-independent Schrödinger equation results according to the expression:

$$J_{tot}=-q\hbar\sum_k W(k)\,\mathrm{Im}\left(\psi_k^*(x)\frac{1}{m^*(x)}\frac{\partial\psi_k(x)}{\partial x}\right), \quad (9)$$

where a superposition over suitably normalized quantum states $\psi_k$ is performed.

### C. Capacitance calculation

The capacitance of the quantum well varactors can be represented by the device small signal capacitance

$$C=\frac{\partial Q_{dipole}}{\partial V_{bias}}, \quad (10)$$

where the charge $Q_{dipole}$ is the dipole charge integrated over the depletion side of the device. We note that for structures with a uniform doping outside the barrier/well region, only one charge dipole exists, and integration over either side of the dipole yields the correct capacitance value. However, for a nonuniform doping profile such as the one for TBDW varactors, multiple charge dipoles exist and care must be used to define the integration domain. In the device structure (shown in Fig. 3), the thin, highly-doped $N^+$ regions next to the undoped spacers will be referred to as $\Delta$ regions for convenience. If we draw a Gaussian surface enclosing the left contact region, and let it advance toward the barrier/well, the net charge enclosed by the surface at zero bias will be zero at the $N^-$ layer, positive at the $\Delta$ region, and zero again at the right of the spacer. For the present structure, the charge dipole for the capacitance evaluation is considered to be divided by the barrier-spacer interface at the right hand side. When the left contact is biased as the cathode, the charge integration is then taken to include all the points at the right-hand side of the barrier/well region, abbreviated as RHS. The dipole charge is then given by:

$$Q_{dipole}=\int_{RHS}q(x)dx, \quad (11)$$

where $q(x)$ is the net charge density at $x$, obtained from the self-consistent calculation. The physical significance of this integration will be illustrated when the calculated charge and potential distributions for various bias voltages are displayed in Sec. IV.

## III. DEVICE DESIGN AND FABRICATION

### A. Device design

The above procedure was used to model the $C$-$V$ and $I$-$V$ characteristics of various types of quantum well varactors. The calculated $C$-$V$ curves for two varactor structures (a SBV and a superlattice varactor) are shown in Fig. 2. For a SBV with the structure of GaAs/AlAs(200 Å)/GaAs, the calculated capacitance ratio ($C_{max}/C_{min}$) is about 2 [Fig. 2(a)], comparing favorably with the experimental $C$-$V$ curve of the SBV in Fig. 1. Note also that the SBV diodes usually suffer from rather large leakage current density due to tunneling from the $\Gamma_{GaAs}$ to $X_{AlAs}$ valleys. For a superlattice varactor (SLV), which has a structure of GaAs/SL/GaAs, with the SL consisting of 10 periods of AlAs(20 Å)/GaAs(20 Å), the leakage current density is significantly supressed due to the effect of the Wannier–Stark ladder.[11] However, since the change of depletion width under bias is insignificant compared with the SL width for this particular structure, the calculated capacitance ratio is less than 3 [Fig. 2(b)], in agreement with our initial experimental data.

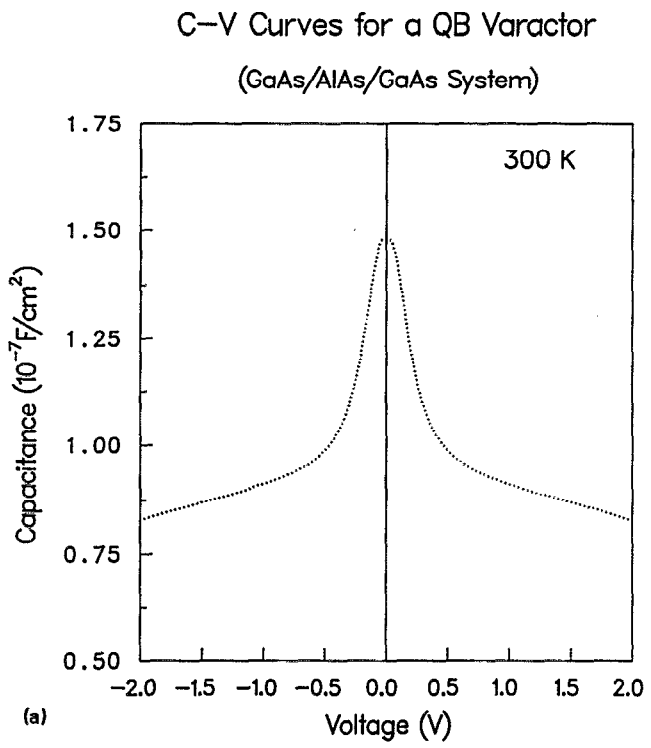


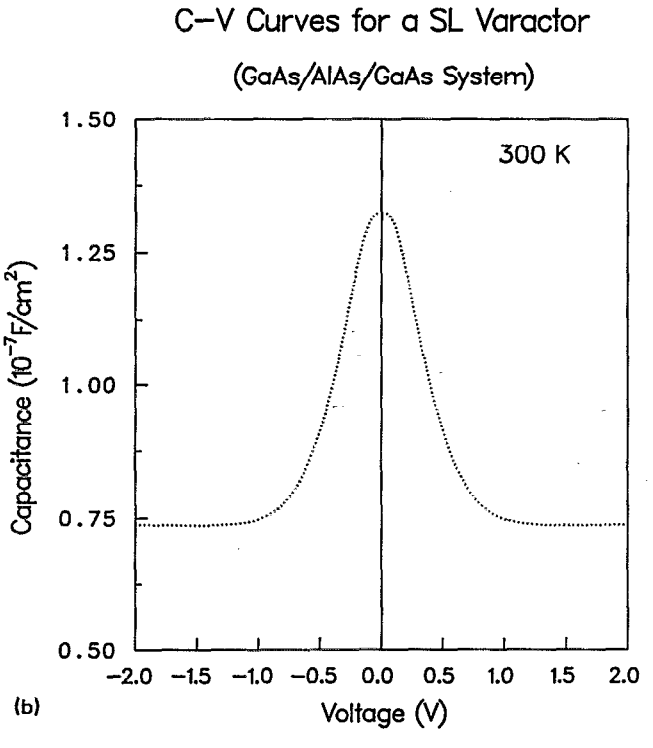


FIG. 2. Calculated *C-V* characteristics for (a) SBV and (b) SLV using this model.

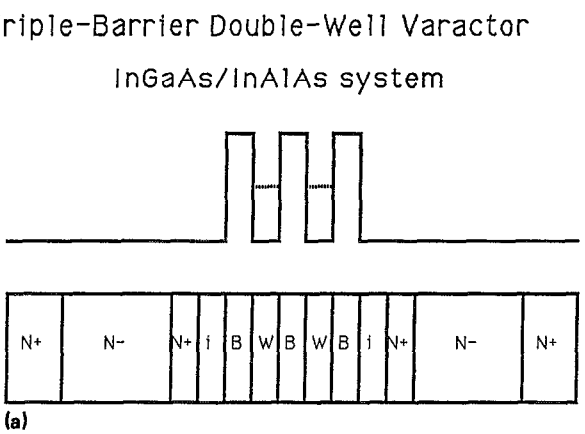


| | |
|---|---|
| N+ InGaAs | 4000 Å |
| N InGaAs | 1000 Å |
| N+ InGaAs | 80 Å |
| i InGaAs | 100 Å spacer |
| i InAlAs | 40 Å barrier |
| i InGaAs | 40 Å well |
| i InAlAs | 40 Å barrier |
| i InGaAs | 40 Å well |
| i InAlAs | 40 Å barrier |
| i InGaAs | 100 Å spacer |
| N+ InGaAs | 80 Å |
| N InGaAs | 1000 Å |
| N+ InGaAs | 4000 Å |

(b)

FIG. 3. (a) TBDW structure showing the conduction band edge, and (b) MBE-grown layers used for TBDW varactor fabrication.

In order to improve the varactor performance, the following design ideas were implemented: (1) the single barrier should be split into multiple barriers and quantum wells to suppress the $\Gamma$-$X$ valley current or the current tunneling through the resonant energy levels in the case of double barrier quantum well structures; (2) the maximum and minimum capacitances should be separately controlled, so that more design freedom can be obtained; (3) the bias voltage at which the transition occurs between the maximum and minimum capacitances can be controlled by the sheet charge density and the thickness of the $\Delta$ layers; (4) the number of barriers/wells can be optimized in terms of the requirement of capacitance ratio, series resistance, and acceptable leakage current density.

The TBDW varactor we designed and fabricated has a lattice-matched InGaAs/InAlAs structure, with the layers shown in Fig. 3(b). The structure is designed such that, at zero bias, the $\Delta$ regions are not fully depleted and the device capacitance is approximately the capacitance of the TBDW ($C_0$). Under a small bias voltage, however, as one $\Delta$ region is fully depleted, the device capacitance is reduced to the capacitance ($C_1$) between an accumulation layer on one side of the barrier/well region and the contact on the other side. Since $C_1$ can be designed to be much smaller than $C_0$, very high capacitance ratio can be obtained. Also,

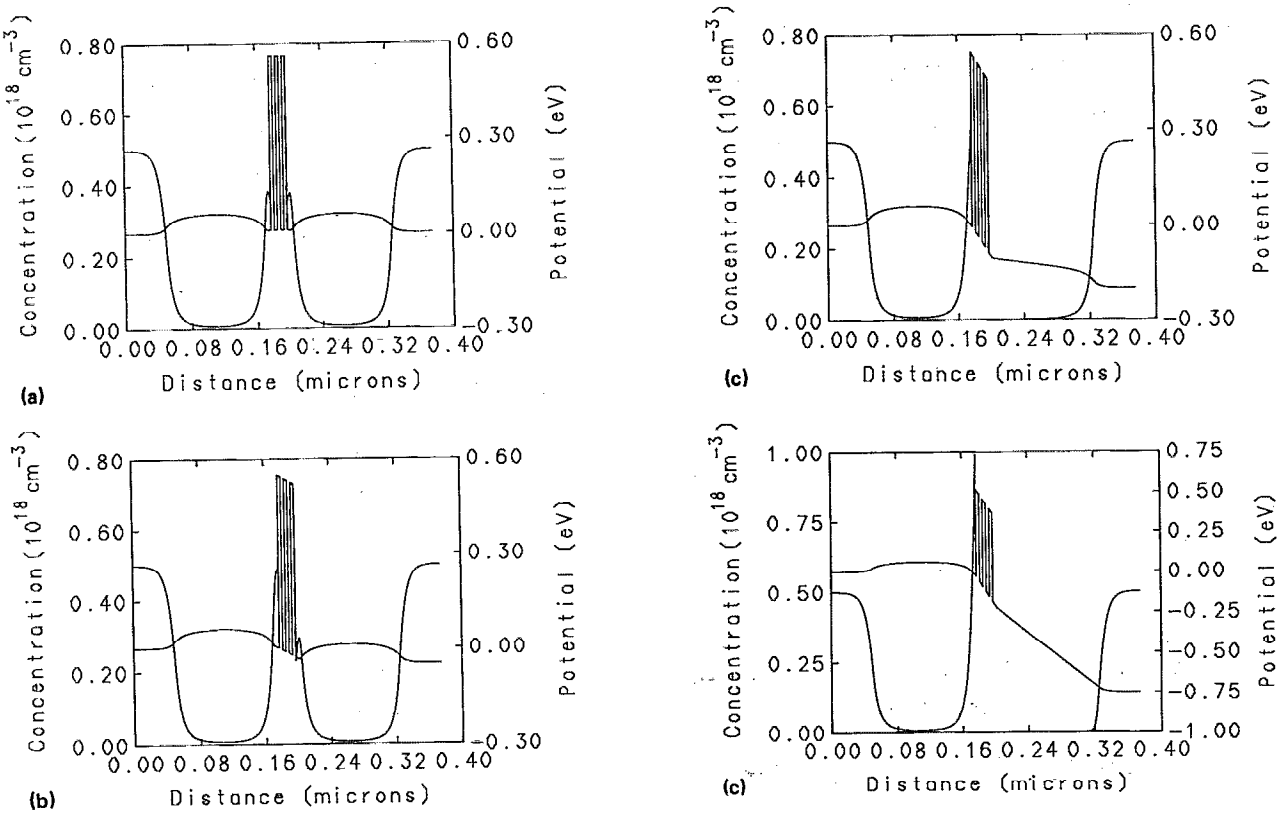


FIG. 4. Charge and potential distributions of the TBDW varactor under (a) 0, (b) 0.05, (c) 0.2, and (d) 0.75 V bias voltages.

the bias voltage at which the sharp drop in capacitance occurs can be designed by applying Gauss's law to the charge in the Δ regions. These features can be seen from the calculated energy and charge distributions shown in Sec. IV.

### B. Device fabrication

The $In_{0.53}Ga_{0.47}As$ and $In_{0.52}Al_{0.48}As$ layers for the device structure were grown at a substrate temperature of 520 °C using a Riber MBE reactor. A 500 Å InGaAs buffer was grown on a (100) $n^+$ InP substrate to reduce defects and silicon was used for the $n$-type dopant. The device fabrication was carried out using a standard diode process. An image reversal process was used to achieve the liftoff of the frontside Ni/Ge/Au/Ti/Au contact metals, and wet selective etching was used to form diode mesas. The diameter of the diodes ranges from 90 to 10 $\mu$m. The $C$-$V$ and $I$-$V$ curves of the TBDW varactor were measured in a cryogenic cooling stage at 80 K. The measured data were taken on the 90 $\mu$m devices.

## IV. RESULTS AND DISCUSSION

### A. Charge and potential distributions

The electronic charge and potential ($E_c$) distributions at various bias voltages are shown in Fig. 4, where the bias voltage applied across the diode can also be found from the potential difference between the contacts. For this structure, under zero bias, the charge and potential distributions are symmetrical. The zero-bias capacitance ($C_0$) is then due to the electronic charge at the spacer regions. For the structure under consideration, the space charge inside the barrier/well region is negligible, $C_0$ is essentially the parallel plate capacitance determined by the thickness of the barrier/well region and can be designed to be large enough to suppress the leakage current. However, for structures involving deep quantum wells, the bound state charge inside the quantum wells can contribute significantly to the capacitance evaluation. Note that the electronic charge in the Δ regions is lower than the local doping level because the thickness of the Δ layer is not sufficient to allow the charge to reach its equilibrium value.

When a 0.05 V bias is applied between the left and right contacts, electrons are injected from the left contact, resulting in an electron accumulation at the LHS; the electrons at the RHS are extracted into the right contact, resulting in a surplus of positive charge at the RHS. This is shown in Fig. 4(b) where the electronic charge density is rapidly decreasing and an electric field is established across the barrier/well region.

When the bias voltage is increased to 0.2 V, the electronic charge at the RHS in the spacer and Δ layers is essentially depleted [Fig. 4(c)]. The accumulated electronic charge at the LHS must now be balanced by the positive charge at the $N^-$-$N^+$ region at the right contact. The capacitance of the device ($C_1$) at this bias voltage is now due to the accumulated electronic charge at the LHS and the positive charge (ionized donors) at the right con-

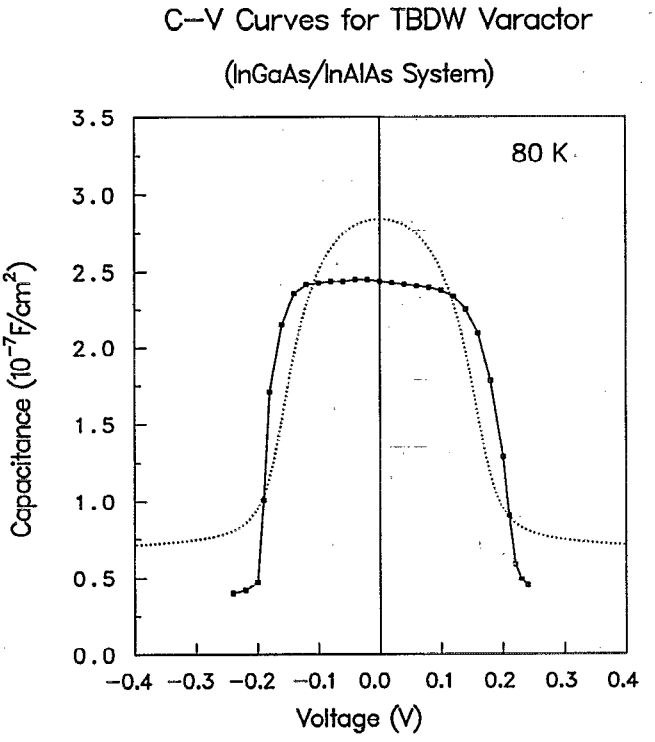


FIG. 5. Calculated (dotted line) and measured (solid line with dots) *C-V* characteristics of TBDW varactor.

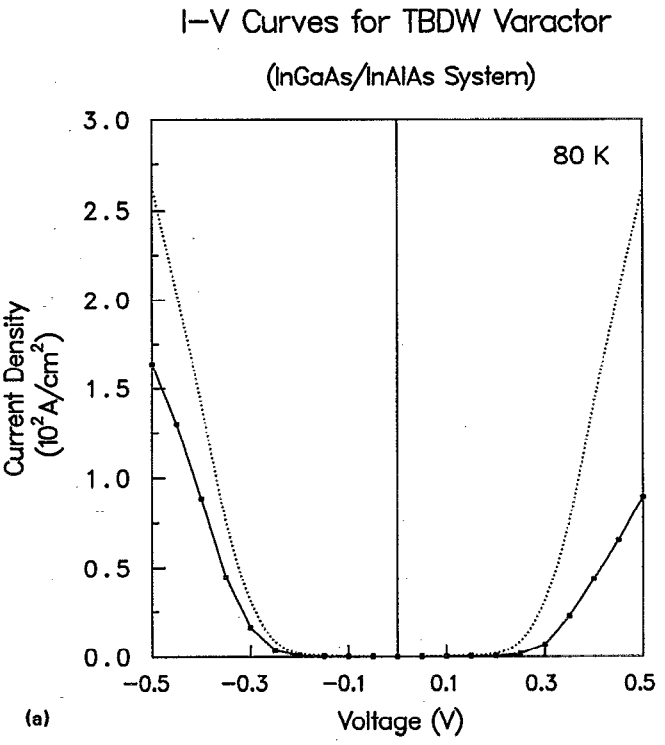


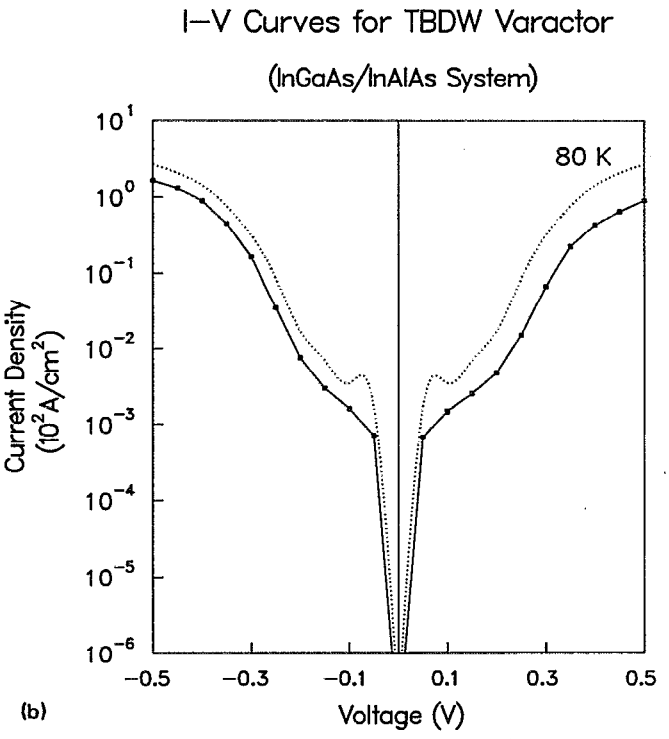


FIG. 6. Calculated (dotted line) and measured (solid line with dots) *I-V* characteristics of TBDW varactor. (a) current density in linear scale, (b) current density in logarithmic scale.

tact being separated by the thick $N^-$ layer. The device capacitance is thus approaching its minimum value ($C_{min}$).

As the bias voltage is further increased [Fig. 4(d)], more positive charge will be needed at the right contact, but the depletion width at the RHS will only increase slightly since the right contact is heavily doped. The device capacitance is therefore approximately constant at its minimum value.

### B. *C-V* and *I-V* characteristic of the TBDW devices

The calculated and measured *C-V* and *I-V* characteristics at 80 K are shown in Figs. 5 and 6, respectively. Comparing the calculated and measured capacitances, very good agreement between the theoretical model and experimental data is achieved with $C_{max}/C_{min}$ typically greater than 5 within a small bias range of $\pm 0.2$ V, as designed. The measured *C-V* curve, however, has nonideal symmetry and a flat capacitance region for small bias. The nonideal symmetry is probably due to the nonideal doping profile near the $\Delta$ regions, while the flat region may indicate that the total amount of charge in the $\Delta$ layers is more than required. The onset of the constant capacitance region in the measured curve is just visible with the slope changing at about 0.2 V; the leakage current beyond that point is too large to allow a reliable capacitance measurement.

The results for the current density in Fig. 6 also show very good agreement between the calculated and measured curves. However, the current density calculation includes a number of simplifications in addition to the effective mass approximation. First, the leakage current through the possible impurity states in the barriers as well as the leakage through possible surface states have been ignored. Second, our model does not include scattering mechanisms and therefore cannot model possible current transport through the $X$ valleys[12,13] and other scattering-related processes. We expect that our current calculation will deviate more

from the experimental values for structures with a thick (greater than $\sim 200$ Å[14]) barrier or several more barriers. Further work is desired to improve the current density calculation for such structures.

## V. CONCLUSION

A theoretical model was presented for modeling the $C$-$V$ and $I$-$V$ characteristics of quantum well varactors. The calculated results compared favorably with the experimental data. The model was shown to be very useful for design and optimization of quantum well varactors.

A TBDW varactor was successfully designed and fabricated that exhibits superior capacitance ratio (typically $\sim 5$ or greater) within a very small bias range ($\sim \pm 0.2$ V) with an acceptable current density level. The Wannier–Stark ladder is effectively utilized in the TBDW varactor to suppress the leakage current, while the Δ-doped layers control the transition from maximum to minimum capacitance. Since the maximum and the minimum capacitance of the device can be controlled separately, design optimization of multiple quantum well varactors can be readily performed for specific applications. On the other hand, further improvement of the current calculations is desired to include effects such as the $\Gamma - X$ transport.

## ACKNOWLEDGMENTS

The authors wish to thank Professor P. Bhattacharya and Y. C. Chen for providing the MBE materials used in this study. This work was supported by the Army Research Office under the URI program Contract No. DAAL03-87-0007.

[1] E. Kollberg and A. Rydberg, Electron. Lett. **25**, 1696 (1989).
[2] T. J. Tolmunen and M. A. Frerking, Theoretical Efficiency of Multiplier Devices, Proceedings of the Second International Symposium on Space Terahertz Technology, edited by F. T. Ulaby and C. A. Kukkonen, Jet Propulsion Laboratory, California Institute of Technology, Pasadena, CA, February 26, 1991, p. 197.
[3] P. D. Batelaan and M. A. Frerking, *Quantum Well Multipliers, Conference Digest for the 12th International Conference on Infrared and Millimeter Waves,* edited by K. J. Button (IEEE, New York, 1987), p. 14.
[4] U. Lieneweg, B. R. Hancock, and J. Maserjian, Barrier-Intrisic-$N^+$ (BIN) Diodes for Near-Millimeter Wave Generation, *ibid.* (1987), p. 6.
[5] W. R. Frensley, *Quantum Kinetic Theory of Nanoelectronic Devices, Proceedings of the International Symposium on Nanostructure Physics and Fabrication,* edited by M. A. Reed and W. P. Kirk (Academic, Boston, 1989), p. 231.
[6] K. L. Jensen and F. A. Buot, J. Appl. Phys. **67**, 7602 (1990).
[7] R. K. Mains, J. P. Sun, and G. I. Haddad, Appl. Phys. Lett. **55**, 371 (1989).
[8] W. B. Joyce and R. W. Dixon, Appl. Phys. Lett. **31**, 354 (1977); C. Kittle and H. Kroemer, *Thermal Physics,* 2nd ed. (Freeman, San Francisco, 1986).
[9] R. K. Mains, J. P. Sun, and W. L. Chen, "Extension of the Joyce-Dixon Approximation for Semiconductor Device Modeling within the Thomas–Fermi Approximation" (unpublished).
[10] J. P. Sun and R. K. Mains (unpublished).
[11] G. H. Wannier, Rev. Mod. Phys. **34**, 645 (1962).
[12] M. Rossmanith, J. Leo, and K. von Klitzing, J. Appl. Phys. **69**, 3641 (1991).
[13] H. C. Liu, Superlattices and Microstructures **7**, 35 (1990).
[14] H. Sakaki, T. Matsusue, and M. Tsuchiya, IEEE J. Quantum Electron. **25**, 2498 (1989).